Three-Dimensional Tracking of Single Secretory Granules in Live PC12 Cells

Dongdong Li,* Jun Xiong,* Anlian Qu,* and Tao Xu*†
*Institute of Biophysics and Biochemistry, School of Life Science and Technology, Huazhong University of Science and Technology, Wuhan 430074, People's Republic of China; and †National Laboratory of Biomacromolecules, Institute of Biophysics, Chinese Academy of Sciences, Beijing 100101, People's Republic of China

ABSTRACT Deconvolution wide-field fluorescence microscopy and single-particle tracking were used to study the three-dimensional mobility of single secretory granules in live PC12 cells. Acridine orange-labeled granules were found to travel primarily in random and caged diffusion, whereas only a small fraction of granules traveled in directed fashion. High K^+ stimulation increased significantly the percentage of granules traveling in directed fashion. By dividing granules into the near-membrane group (within 1 μm from the plasma membrane) and cytosolic group, we have revealed significant differences between these two groups of granules in their mobility. The mobility of these two groups of granules is also differentially affected by disruption of F-actin, suggesting different mechanisms are involved in the motion of the two groups of granules. Our results demonstrate that combined deconvolution and single-particle tracking may find its application in three-dimensional tracking of long-term motion of granules and elucidating the underlying mechanisms.

INTRODUCTION

Vesicular trafficking constitutes a major means for intracellular and transmembrane cargo transportation. For example, hormones and neurotransmitters are stored in vesicles and are released upon fusion with the plasma membrane. Before a vesicle can fuse with the plasma membrane, it has to undergo a series of steps such as budding, translocation, tethering, docking, and priming (Pfeffer, 1999; Toonen and Verhage, 2003; Jahn et al., 2003). To better understand the mechanisms of different steps in vesicular trafficking, it is desirable to directly visualize the movement of vesicles inside living cells.

Two-dimensional (2-D) confocal microscopy has been used to explore granule movement in single optical section (Pouli et al., 1998; Levitan, 1998). The contribution from the missing z direction is ignored by assuming that observed granules move within the observation plane during the experimental time. Three-dimensional (3-D) single-particle tracking (SPT) in living cells has been difficult for confocal fluorescence microscopy. This probably is due to low time resolution inherited with the laser scanning, high photobleaching, and toxicity at the expense of low light collection efficiency. Recently developed total internal reflection fluorescence microscope (TIRFM) has proved very successful in studying the movement of single granules. The advantages of low background, high temporal resolution, minimal photobleaching, and phototoxicity have made TIRFM very popular in tracking the docking and fusion of granules (Steyer and Almers, 1999; Oheim and Stühmer, 2000; Ohara-Imaizumi et al., 2002). However, as the penetration depth of the evanescent field is limited to several hundreds of nanometers, TIRFM can only be employed to study granules right underneath the plasma membrane close to the coverglass-solution interface, whereas granules residing deeper inside the cytosol are invisible under TIRFM. It is unclear whether the ''unphysiological'' adhesion of cell membrane to the coverglass will have an impact on the mobility and function of secretory granules. On the other hand, although TIRFM is generally used for 2-D tracking, z-mobility can be indirectly inferred from the changes in the intensity of fluorescence (Ölveczky et al., 1997; Johns et al., 2001). However, since TIRFM is extremely sensitive to the objects' vertical movement, fluctuation in fluorescence unrelated to changes in axial position (such as variation in excitation power, quenching, or dequenching of fluorescence due to pH change, etc.) will result in misinterpretation of the z-position.

To avoid the restriction of TIRFM in observing only the cell-glass interface and to expand our knowledge on 3-D movement of granules throughout living cells, we have constructed a system to combine deconvolution wide-field fluorescence microscopy (WFFM) and 3-D single-particle tracking technique. We have employed this method to study the 3-D mobility of single granules in living PC12 cells. Indeed, 3-D mobility of granules distant from the plasma membrane has yet to be demonstrated. We have compared the mobility of granules that are either close to the plasma membrane (GP) or located deep inside the cytosol (GC). Our data illustrated that the mobility of internal granules is greater than those near the plasma membrane. Whereas the majority of granules wander in random and caged fashion, stimulation increases significantly the percentage of granules that travel in a directed fashion. We also found that the mobility of GP is more prone to the disruption of F-actin,

Submitted March 19, 2004, and accepted for publication May 25, 2004.

Address reprint requests to Tao Xu, E-mail: txu@mail.hust.edu.cn; or Anlian Qu, E-mail: alqu@mail.hust.edu.cn.

0006-3495/04/09/1991/11 $2.00

doi: 10.1529/biophysj.104.043281

whereas that of GC is less affected. Our results demonstrate that combining deconvolution and 3-D SPT is useful in following the long-term 3-D movement of single granules within living cells.

MATERIALS AND METHODS

Cells, labeling, and solutions

PC12 cells were cultured as described (Lang et al., 1997). Cells were used shortly after being transferred to homemade coverslip chambers. Granules were labeled by incubating the cells in a buffer containing 3 μM acridine orange (AO) (Molecular Probes, Eugene, OR) for 15 min at 21°C. Then the cells were washed twice in dye-free buffer, which contained (in mM): 150 NaCl, 5.4 KCl, 2 $MgCl_2$, 1.8 $CaCl_2$, and 10 HEPES (pH 7.4). Cells were viewed ~60 min later. To verify our determination of the membrane contour, cells were first incubated in normal external solution containing 4 μM FM1-43 (Molecular Probes, Eugene, OR) for 5–10 min until we saw a stable fluorescence staining that was uniformly distributed along the plasma membrane. After locating the plasma membrane, FM1-43 was washed out from the membrane in dye-free buffer, which resulted in a rapid disappearing of the staining. Then, for the same cell we labeled its granules with AO as described above. To avoid unnecessary photobleaching, fluorescence excitation was turned on only during image acquisition. $[K^+]_o$ was raised by local perfusion with a multi-channel perfusion system (MPS-1, YiBo Life Science Instrument, Wuhan, China). The stimulation buffer contained (in mM): 90.4 NaCl, 65 KCl, 2 $MgCl_2$, 1.8 $CaCl_2$, and 10 HEPES (pH 7.4). Sometimes, dense-core granules were labeled by transient transfection with human pro-neuropeptide Y (NPY) (plasmid kindly provided by W. Almers, Vollum Institute, Oregon Health and Science University, Portland, OR) fused to the N-terminal of DsRed, which would be used to compare with AO-labeled granules in size, but not used for successive 3-D imaging due to the longer exposure time required for imaging DsRed labeled granules. Actin cytoskeletons were disrupted by incubating the cells with 5 μM latrunculin B (ICN Biomedicals, Aurora, Ohio) for 2 min.

Image collection

Cells were grown on high refractive-index glass coverslips and viewed under an inverted microscope (IX70; Olympus America, Melville, NY) with a 1.65 numerical-aperture (NA) objective (APO ×100 O HR, Olympus). Excitation light from a fiber optical-coupled monochromator (Polychrome IV; TILL Photonics, Bayern, Germany) was passed through a shutter that opened only during camera exposure. The wavelength selection and shutter were controlled by the image acquiring software (TILL vision 4.0, Till Photonics). Images were acquired with a cooled charge-coupled device (PCO SensiCam, Kelheim, Germany) with pixel size of 0.067 μm at the specimen plane. Appropriate dichroic mirror (505 DCLP from Chroma Technology, Brattleboro, VT) and emission filter (535LP from Chroma) were used for imaging. A series of 2-D images were collected via moving the focal plane through a cell with the piezoelectric z axis controller (E-662. LR, Physik Instrumente, Karlsruhe, Germany). The focal plane advanced ~75% of the distance moved by the objective due to the discrepancy in refractive index between the immersion oil and cytosol. Accordingly, we reconstructed 3-D images of cells with those stacks of 2-D sections. For obtaining successive 3-D images of a cell, we selected the plane where the outmost edge of the cell appeared sharpest as the reference plane. Starting from the reference plane, we sampled sixteen 2-D sections with 0.2 μm stepping size to generate one 3-D image. An illustration of the imaged region is shown in Fig. 1 *D* between the dashed lines. As to the same imaged region, we successively recorded its 3-D images every 5 s for 70 s to generate a stack including fifteen 3-D images. In our imaging protocol, exposure time for each optical section was 5 ms, and the waiting interval for the next section was 170 ms. Occasionally, more sections were sampled to include the whole cell.

Point spread function and deconvolution

Knowing the point spread function (PSF) of the imaging system is the prerequirement for deconvolution. For our 1.65-NA objective, we determined the 3-D PSF through either experimental or theoretical method. In experimental measurement, we dried subresolution fluorescent beads (PS-Speck; diameter, 0.175 μm; Molecular Probes) on the coverslip (refractive

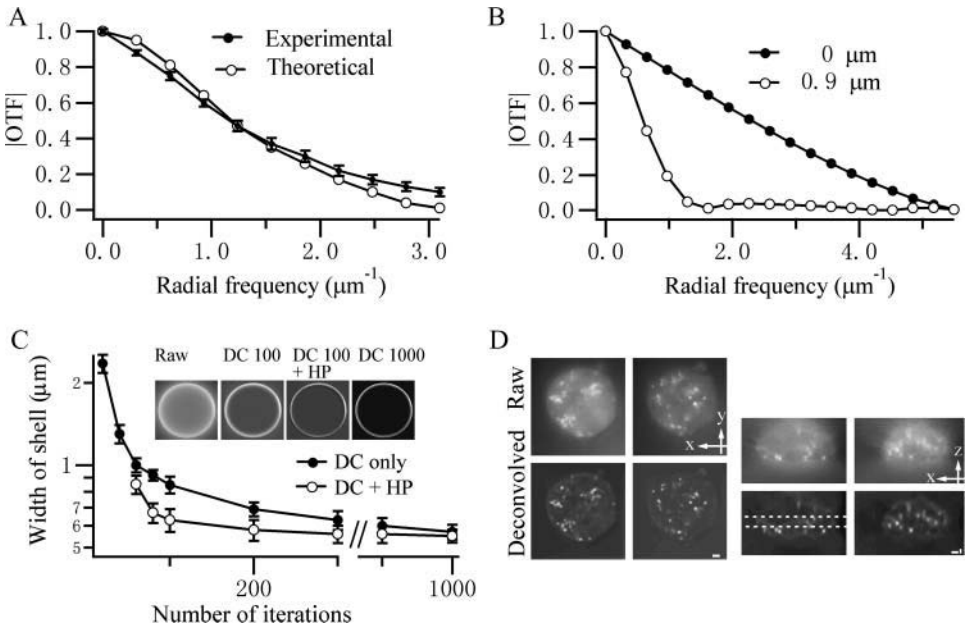

FIGURE 1 Point spread function and deconvolution. (*A*) Comparison of |OTF (u, v)| distribution of corresponding equal-defocus (0.4 μm) optical sections between experimental and theoretical PSF. Experimental PSF was averaged from eight measurements, which gave quite similar OTF as that of theoretical PSF ($P = 0.98$, KS test). (*B*) OTF distribution of the point light source from different defocus sections on the focal plane. (*C*) Evaluation of deconvolution result using different iterations and high-pass filtering; 15-μm beads with a spherical shell of fluorescence ~0.5–0.7 μm thick were used for the evaluation. Equatorial sections were used to measure the width of the shell ($n = 7$ beads). Deconvolution removes the out-of-focus blur and gives better estimates of the width. DC stands for deconvolution, and HP for high-pass filtering at a spatial frequency of 1/μm. (*D*) Selected deconvolved 3-D images of a PC-12 cell from stacks of images, wherein secretory granules were labeled by AO. Left panel, lateral sections with a distance of 1 μm in z direction. Right panel, axial sections with a distance of 3 μm in y direction. Dashed lines depict the 3-D region we sampled for analysis at a z-step interval of 0.2 μm. Scale bars, 1 μm.

index, 1.78; thickness, 0.15 mm; Olympus) and then collected its 3-D images at different focal distances. According to the parameters of our imaging system, the theoretical PSF was derived from the mathematic model described in Gibson and Lanni, 1991.

The iterative expectation-maximum algorithm based on a maximum-likelihood approach (Conchello and McNally, 1996) was used to deconvolve every recorded 3-D fluorescence image. The deconvolution algorithm used in our study was regularized with intensity regularization that can avoid the appearance of some artificial bright spots in deconvolved images (Conchello and McNally, 1996; Markham and Conchello, 1997). To verify the result of deconvolution, we employed a well-defined 3-D specimen, FocalCheck Fluorescent Microsphere from Molecular Probes. The bead is a spherical shell of fluorescence with a thickness of 0.5–0.7 μm as provided by Molecular Probes.

Evaluation of 3-D SPT with simulation

2-D SPT has been widely applied to monitor subpixel displacements of individual fluorescence particles between successive images, and some evaluation frameworks have been performed (Gosh and Webb, 1994; Kues et al., 2001; Cheezum et al., 2001; Thompson et al., 2002). The rationale of subpixel displacement detection is that fluorescence of single particles spreads over more than one pixel in recorded images, so the subpixel displacement can be tracked by weighting the fluorescence distribution from multiple pixels between successive time-lapse images. Here, we calculated centroids of successive images to estimate subpixel displacements in three dimensions. The centroid of a single axis is

$$C_x = \sum_{i=1}^{m}\sum_{j=1}^{n}\sum_{k=1}^{t}(x_i \times I_{ijk}) \Big/ \sum_{i=1}^{m}\sum_{j=1}^{n}\sum_{k=1}^{t} I_{ijk}, \qquad (1)$$

in which x_i is the coordinates of a pixel on the x axis, and I_{ijk} denotes the fluorescence intensity of the corresponding pixel. A threshold was defined as the fraction of the maximum fluorescence intensity, and those normalized pixels below the threshold were appointed zero. We applied computer-generated granule trajectories and movement, based on the measured parameters, to assess the influences of different signal/noise ratios (SNRs) and thresholds on SPT performance. The simulated granule, with similar size with actual granules (120 nm in diameter, Tooze et al., 1991), was initially created in one high-resolution matrix whose cell size was 0.01 μm $\times$ 0.01 μm $\times$ 0.03 μm (x, y, z), which was then convolved with the 3-D PSF mentioned above. The simulated CCD image was acquired by covering the same physical extent of the PSF-convolved high-resolution matrix with a low-resolution matrix whose cell size was set to 0.07 μm $\times$ 0.07 μm $\times$ 0.15 μm (x, y, z), which approximates the real sampling size used in our experiments. Subsequently, shot noise after a Poisson distribution was added for every pixel. For a particular SNR, several stacks, each of which contained sequential 3-D images of the simulated granule, were generated with computer. Subpixel displacements of the simulated granule between successive 3-D images were achieved through randomly moving granule along three dimensions in high-resolution matrix.

The mean-square displacement (MSD) is of critical importance for assessing the parameters of granule's 3-D mobility, so we evaluated the performance of our SPT algorithm for estimating the MSD of the simulated granule at different SNR levels. The resemblance between SPT-estimated MSD and the actual one was assessed by the P-values given in the Kolmogorov-Smirnov (KS) test. For every given SNR, the optimized threshold for each simulated granule tracking was determined by maximizing the P-values (see Fig. 2). In addition, the bias and standard deviation (STD) was calculated and used as another indication of tracking accuracy for the selection of appropriate threshold:

$$bias = \langle a - \hat{a} \rangle \quad STD = \left\langle (a - \langle a \rangle)^2 \right\rangle^{1/2}. \qquad (2)$$

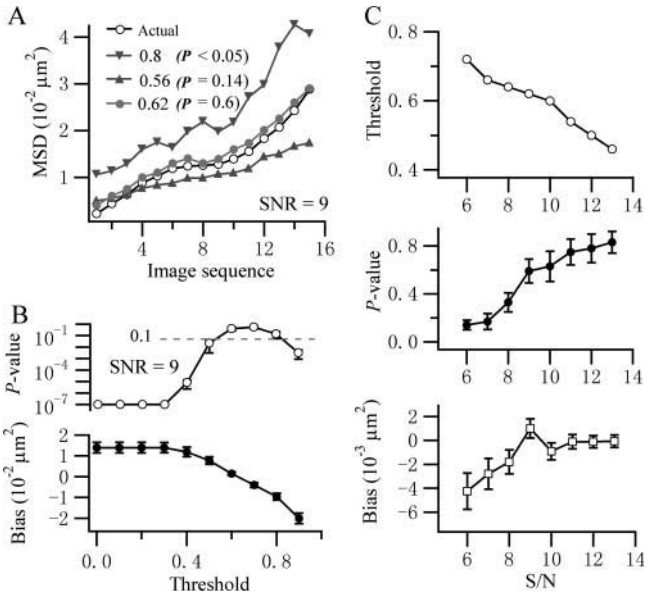

FIGURE 2 SNR and threshold selection are critical for the performance of SPT. (*A*) Simulated granule (with SNR = 9) trajectories based on measured parameters were used to evaluate the influence of different threshold levels (labeled in figure) on the estimation of MSD. The resemblance between SPT-estimated MSD and the actual one was assessed by the P-values given in the Kolmogorov-Smirnov (KS) test, with a maximum P-value indicating the best resemblance. (*B*) Assessing mean P-values and bias between estimated and actual MSD under different threshold levels for SNR = 9 (n = 7 simulated trajectories). Dashed line indicates a P-value of 0.1. The maximum P-value is attained at a threshold of 0.62. (*C*) Threshold selection is dependent on the SNR of each granule. For every given SNR, the optimized threshold for each simulated granule tracking was determined by maximizing the P-values. Averaged maximal P-values and the corresponding biases are displayed against different SNRs. Larger SNRs give better SPT performance with larger P-values and less biases.

Error for the bias was given with STD for a given threshold. Both SPT and simulation program were written in MATLAB 6.1.

Mobility analysis of granules residing in different subcellular regions

For comparing the mobility of granules residing close to the plasma membrane and the ones that are deep inside the cytosol, we divided the total population of granules into two groups according to their relative distances from the plasma membrane. One group included granules localized <1 μm from the contour of the plasma membrane, termed GP. The rest of granules inside the cytosol were termed GC. The edge-detecting algorithm (first described by Canny, 1986) implemented in MATLAB 6.1 software was employed to detect the membrane contour from the deconvolved image of AO-loaded cells (see Results section for more details).

The mobility of each granule can be analyzed by determining its MSD as a function of time interval $n\Delta t$. MSD in three dimensions can be calculated as follows:

$$MSD(n\Delta t) = \frac{1}{N-n}\sum_{j=1}^{N-n}\{[x(j\Delta t + n\Delta t) - x(j\Delta t)]^2 + [y(j\Delta t + n\Delta t) - y(j\Delta t)]^2 + [z(j\Delta t + n\Delta t) - z(j\Delta t)]^2\}, \qquad (3)$$

where $n = 1,2.\ldots.(N-1)$, N is the total number of images in the recorded sequence, Δt is the time interval between two successive 3-D images in a stack, $x(j\Delta t)$, $y(j\Delta t)$ and $z(j\Delta t)$ are the coordinates of the granule at time $j\Delta t$, and $x(j\Delta t + n\Delta t)$, $y(j\Delta t + n\Delta t)$, and $z(j\Delta t + n\Delta t)$ are the coordinates of the granule in another image taken $n\Delta t$ later.

For random diffusion, granules move with a single 3-D diffusion coefficient ($D^{(3)}$):

$$\mathrm{MSD}(n\Delta t) = 6D^{(3)}(n\Delta t). \quad (4)$$

In directed diffusion, a drift velocity $V^2 = v_x^2 + v_y^2 + v_z^2$ is superimposed on random diffusion:

$$\mathrm{MSD}(n\Delta t) = 6D^{(3)}(n\Delta t) + V^2(n\Delta t)^2. \quad (5)$$

The feature of diffusion limited in a cage, termed caged diffusion, can be characterized by the following approximate equation (Saxton and Jacobson, 1997):

$$\mathrm{MSD}(n\Delta t) = R^2[1 - A_1 \exp(-6A_2 D^{(3)} n\Delta t/R^2)], \quad (6)$$

where $A_1 = 0.99$ and $A_2 = 0.85$, and R is the radius of the spherical cage in which the particle is free to diffuse with $D^{(3)}$. To distinguish the proportion of granules diffusing with different fashions, we analyzed granules by fitting their MSDs with Eqs. 4–6 and then selected the best fits by KS test, and sometimes with the assistant of χ^2 value. The scope of movement of a granule is defined as the mean value of its displacements in three dimensions during the observation period.

Statistics

For normally distributed data, population averages were expressed as mean ± SE unless otherwise stated, and statistic significance was assessed by the Student's t-test. STD was used in Fig. 3 C. Skewed distribution was confirmed by Fisher equation (Becherer et al., 2003). The median and median standard error (MSE) was used to describe skewed distributed data. Statistical significance of the difference between two skewed distributions was assessed with KS test, χ^2 value, or both. $P < 0.05$ and $P < 0.01$ were denoted as * and **, respectively.

RESULTS

Deconvolution reduces out-of-focus fluorescence in WFFM images

We first determined the experimental and theoretical PSF of our 1.65-NA objective as described in the Materials and Methods section. For quantitative comparison of the experimental and theoretical PSF, we calculated and compared the optical transfer function (OTF) of each section planes based on the respective PSFs. We found that the |OTF| of experimental PSF at given section planes agreed quite well with that of theoretical PSF. As shown in Fig. 1 A, the |OTF|s at defocus of 0.4 μm for the two PSFs were quite similar ($P = 0.98$, KS test). Similar analyses were done for sections with defocus <1 μm. We have further confirmed that MSD plots calculated from images processed with either experimental or theoretical PSF are quite similar (data not shown). Thus, for simplicity, we employed theoretical PSF for subsequent deconvolution calculation. Next, we evaluate how point light sources at different axial planes influence the image of focal plane. As depicted in Fig. 1 B, when a point light source is relatively far from the focal plane (*open circle*), it contributes mainly to the low spatial frequency signals at the focal plane; whereas high spatial frequency fluorescence comes mainly from light sources at adjacent

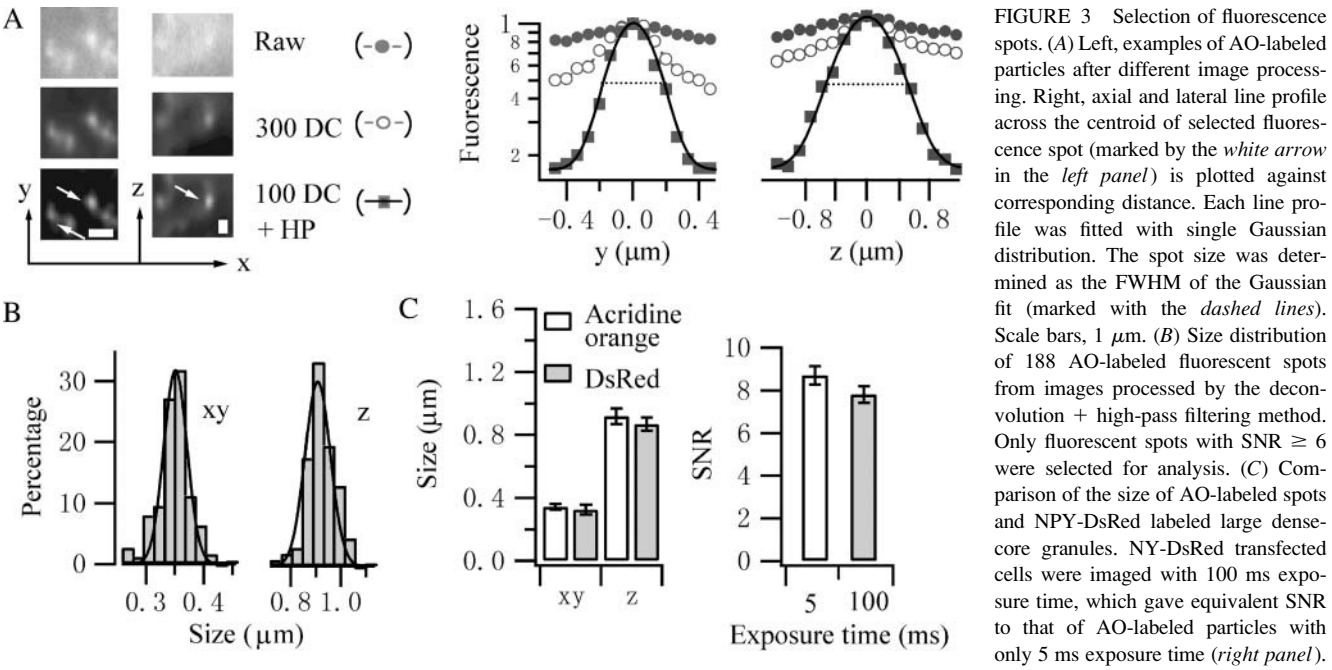

FIGURE 3 Selection of fluorescence spots. (A) Left, examples of AO-labeled particles after different image processing. Right, axial and lateral line profile across the centroid of selected fluorescence spot (marked by the *white arrow* in the *left panel*) is plotted against corresponding distance. Each line profile was fitted with single Gaussian distribution. The spot size was determined as the FWHM of the Gaussian fit (marked with the *dashed lines*). Scale bars, 1 μm. (B) Size distribution of 188 AO-labeled fluorescent spots from images processed by the deconvolution + high-pass filtering method. Only fluorescent spots with SNR ≥ 6 were selected for analysis. (C) Comparison of the size of AO-labeled spots and NPY-DsRed labeled large dense-core granules. NY-DsRed transfected cells were imaged with 100 ms exposure time, which gave equivalent SNR to that of AO-labeled particles with only 5 ms exposure time (*right panel*). Error bars represent STD.

optical sections. Thus, applying high-pass filtering to the images could help to remove out-of-focus fluorescence.

Before applying deconvolution to live cell images, we assessed the algorithm using well-defined 15-μm diameter beads with a thin fluorescent shell of 0.5–0.7 μm in width. As would be expected, sections in unprocessed 3-D images of the bead were seriously blurred by out-of-focus light (*inset* in Fig. 1 *C*), and the width of shell was much larger than its actual size. Deconvolution computationally reduced the out-of-focus blurring, and gradually gave better estimates of the width of the shell with increasing iteration times (Fig. 1 *C*). Since low spatial frequency signal ($<1/\mu$m) contributes little to the analysis of the mobility of granules that are generally <1 μm in size (Steyer and Almers, 1999; Oheim and Stühmer, 2000), we first deconvolved time-lapse images with a small number of iterations (100 for this study), and then high-pass filtered them at a spatial frequency of $1/\mu$m. As depicted in Fig. 1 *C*, deconvolution with 100 iterations followed by high-pass filtering at a spatial frequency of $1/\mu$m gave similar estimate of the width of the shell as that of simple deconvolution with 1000 iterations. Thus, for the rest of the image processing, we routinely employed the 100-iteration deconvolution together with high-pass filtering at a spatial frequency of $1/\mu$m. The recorded and processed images from an AO-loaded PC12 cell are displayed in Fig. 1 *D* for comparison.

Accuracy of SPT depends on the SNR and threshold level

Both the SNR of the object and the threshold level applied to the image are critical for the performance of centroid-dependent SPT. In this study, simulated granule trajectories and movement reconstructions, based on measured parameters, were used to evaluate the performance of SPT. We have generated sequential stacks of 3-D images containing single simulated granules at different SNR. Then, we used different SNRs as a parameter and identified the optimized threshold for each granule tracking according to its SNR. For a particular SNR, different threshold selection exerts significant impact on the SPT-estimated MSD as shown in Fig. 2 *A*. The reason is that as lower threshold is applied, too many background fluorescence remains around tracked granules, making the centroid-based SPT insensitive to granule movement and underestimate MSD throughout; whereas high threshold excludes too many pixels critical for the calculation of centroid and induces unexpected variability in the tracking as well as overestimation of MSD. Hence, we have examined the influence of different thresholds on the significance of difference (assayed by the *P*-value in KS test) and the bias between the real MSD and the one estimated from SPT (Fig. 2 *B*). Thus, appropriate threshold should be chosen to maximize the *P*-value and minimize the bias at given SNR. The relationship of optimized thresholds, corresponding *P*-values, and biases versus SNRs is revealed in Fig. 2 *C*. We notice that higher SNRs give better accuracy in SPT. This emphasizes the necessity to choose fluorescence spots with SNR equal to or above 6 for mobility tracking. Based on the SNR of each granule, we selected corresponding thresholds according to Fig. 2 *C*. For intermediate SNRs not simulated, thresholds were chosen by interpolation between the neighboring integer SNRs.

Identification of fluorescence spots

Most near-membrane fluorescence spots in PC12 cells labeled with AO have been identified as single large dense-core granules (Avery et al., 2000). However, as AO tends to accumulate in acidic compartments, it is important to verify that the cytosolic fluorescence spots that we selected for analysis are actually granules. After deconvolving and high-pass filtering the images, we identified fluorescence spots with an SNR equal to or >6 (marked with *arrows* in Fig. 3 *A*) for further analysis. The lateral and axial fluorescence profiles of each selected AO spot were fitted with Gaussian functions, and the full width at half-maximum (FWHM) of the fitted Gaussian function was taken as a measure of the size of particles (one example is shown in Fig. 3 *A*, *right*). Fig. 3 *B* displays the size distributions of 188 fluorescent spots with the peak lateral and axial size at 0.35 ± 0.02 μm and 0.92 ± 0.05 μm (mean $\pm$ STD), respectively. The larger axial size is caused by the relatively lower axial resolution inherited in WFFM. We then compared the averaged size of these fluorescence spots with that of NPY-DsRed labeled large dense-core secretory granules (Lang et al., 2000; Holroyd et al., 2002) with similar SNR and found their sizes were nearly equivalent (Fig. 3 *C*). In fact, the lateral size of our selected fluorescent spots is close to the TIRFM observation of dense-core granules in PC12 cells (Lang et al., 2000). Thus, we verified that the selection criteria seem to restrict most of the remaining fluorescence spots to large dense-core granules. We further selected those fluorescence spots with both lateral and axial size within the mean $\pm$ 2σ of the Gaussian size distribution for further mobility analysis. Compared with NPY-DsRed labeled granules, larger SNR could be obtained for AO-loaded granules during much shorter exposure time (Fig. 3 *C*), so the employment of AO would provide us the ease of labeling, rapid sampling, and less photodamage for imaging live cells.

3-D tracking of single granules in resting cells

Previous studies have suggested that granules diminished in their mobility as they approached the plasma membrane (Steyer et al., 1997; Johns et al., 2001). Also, the dense cortical actin network underneath the plasma membrane might influence the mobility of granules (Oheim and Stühmer, 2000; Lang et al., 2000). To confirm the usefulness

of our 3-D SPT in studying the mobility of granules at different locations inside the cell, we have separated total granules into two groups, GPs and GCs, according to their relative distances from the detected contour of plasma membrane. The membrane contour was detected using the edge-detecting algorithm of Canny (1986). Briefly, it calculates the intensity gradient of images with the derivative of a Gaussian filter and locates the edge by looking for local maximum of the gradient. This method is robust to noise and likely to detect even weak edges. We compared the contour detected from deconvolved AO-stained images with that obtained from FM1-43 staining in the same cell. FM1-43 is not fluorescent in solution, and becomes fluorescent when incorporated into the membrane lipids (Leung et al., 2002; Angleson et al., 1999). As shown in Fig. 4 *A*, the membrane contours recognized from AO- and FM1-43-stained images were quantitatively comparable. The mean absolute difference between the two contours was 0.29 ± 0.02 μm (estimated from four cells) with a maximum and minimum value of 0.42 μm and 0.1 μm, respectively. The same section as in Fig. 4 *A* was high-pass filtered and displayed in high magnification in Fig. 4 *B*. Granules that meet our selection criteria are marked with circles. One granule identified as GP is indicated with an arrow in Fig. 4 *B*. The time-lapse images of this GP in the *x*, *y* and *x*, *z* plane are displayed in Fig. 4 *C*. As shown in Fig. 4 *C*, the granule seems quite consistent in its size and shape. However, sometimes the rotation of the non-spherical granule may change its projection in the 2-D section. Thus, as further evidence that the deconvolution did not introduce severe artifacts in our study, we have calculated the averaged 3-D volume of granules and found little variation between successive images, as demonstrated in Fig. 4 *D*.

Different motion types of granules

Next we studied the mobility of single granules by 3-D SPT. Only AO-loaded granules present for the entire imaging time were chosen for tracking analysis. Occasionally, we observed disappearance of granules in the middle of the image sampling, which might be due to either the ''explosions'' of AO-loaded granules or exocytosis when the granule is close to the plasma membrane. These granules were not included in subsequent analysis. We found that fluorescence decayed with an averaged time constant of 142.8 s due to photobleaching. Thus the images were corrected for photobleaching before analysis. By fitting the MSD plot with appropriate equations, we have identified three types of motion among 246 total granules from 17 cells. A straight line fit to the MSD is indicative of random diffusion, which was generally observed for both GPs and GCs at similar frequency (Fig. 5 *A*). The major portion of the granules seems to move in a confined compartment and exhibit a negative curvature in the MSD plots (Fig. 5 *B*), which manifests a caged diffusion as if the granule is confined in a cage constructed by some neighboring obstruction. The averaged MSD of GC was much larger than that of GP, reflecting that cytosolic and near-membrane granules are probably restricted by different structures. Functional studies have proposed that granules might be transported along some cytoskeletal tracks powered by motor proteins (Kamal and Goldstein, 2000; Rogers and

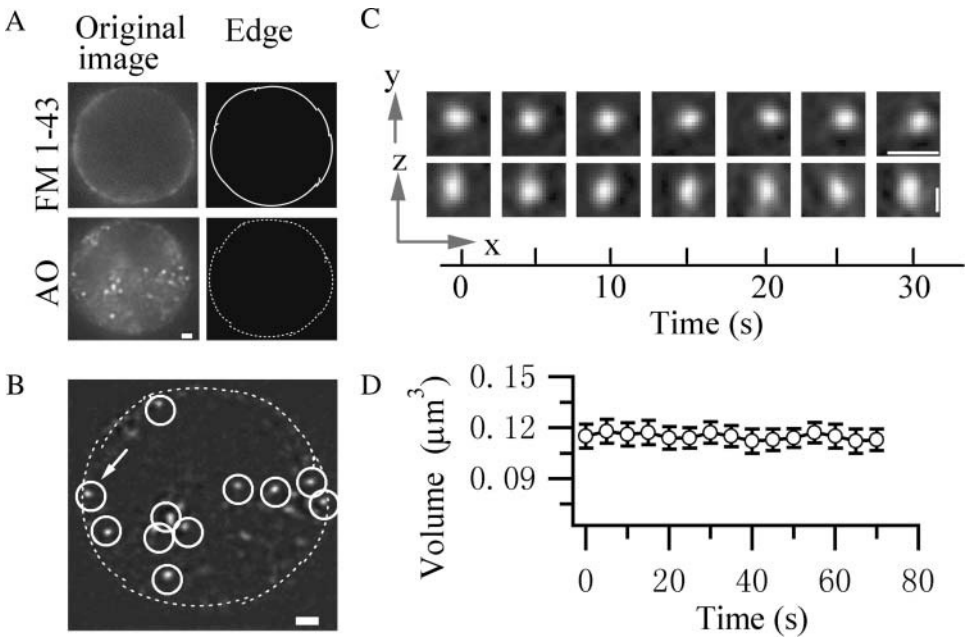

FIGURE 4 3-D tracking of near-membrane granules. (*A*) Membrane position was defined by the edge-detecting algorithm explained in the Materials and Methods section. Membrane contours, detected under AO staining and FM1-43 staining from the same cell, are displayed for comparison. The mean absolute difference between them is 0.29 ± 0.02 μm (data analyzed from four cells). (*B*) The same section as in panel *A* was high-pass filtered and displayed in high magnification. Granules meeting our selection criteria were marked with circles, which were subsequently included in the SPT analysis. (*C*) Sequential images of a granule marked by an arrow in *B*. The radial distance between the centroid of the granule and the membrane is 0.53 μm. Thus, the granule should be considered as a GP according to our definition. Scale bars for panels *A*, *B*, and *C*, 1 μm. (*D*) The averaged volumes from 25 granules calculated from the pixels that exceed the half-maximum fluorescence are displayed as a function of time.

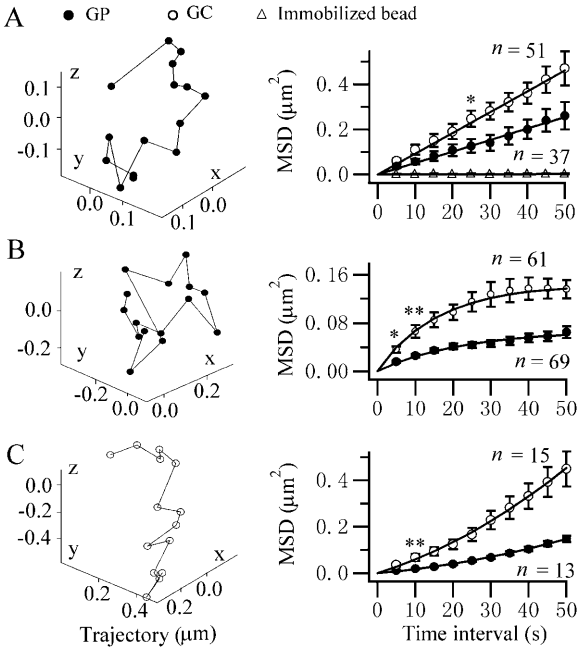

FIGURE 5 Three types of motion exist for both GPs and GCs. Example trajectories (*left*) and averaged MSDs (*right*) of granules that travel in random diffusion (*A*), caged diffusion (*B*), or directed diffusion (*C*) are depicted, respectively. The numbers of granules analyzed are indicated in the graph. For comparison, averaged MSD of six immobilized 175-nm diameter beads imaged under SNR = 6 condition is also displayed. Open circle, solid circle, and open triangle symbolize the GC, GP, and immobilized beads, respectively. * and ** mark the points from which on significant difference exists between the two MSD plots.

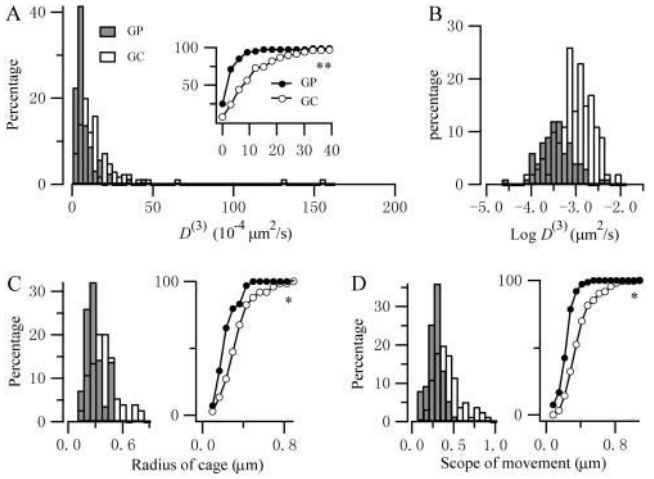

FIGURE 6 Comparison of the mobility between GP and GC. (*A*) $D^{(3)}$ histograms of GP ($n = 119$) and GC ($n = 127$) display a markedly skewed distribution. Inset, cumulative histogram reveals significant difference ($P < 0.01$, KS test). (*B*) $D^{(3)}$ distribution in semilogarithmic presentation. (*C*) Left, distribution of the radius of cage for GPs ($n = 69$) and GCs ($n = 61$) that move in caged diffusion. Right, cumulative histograms reveal significant difference ($P < 0.05$, KS test). (*D*) Scope of movement also displays significant difference ($P < 0.05$, KS test) between GP and GC. For this figure, wave symbols are defined in *A*.

Gelfand, 2000). In our experiments, we have also observed a small portion of both GPs and GCs (~10%) moving along a fixed direction as if transported by some already constructed tracks (Fig. 5 *C*). Their MSD plots resulted in a positive curvature because the V^2 term of Eq. 5 would dominate the MSD for longer time (Fig. 5 *C*). Interestingly, the directed velocity of granule transportation for GC ($15.4 \pm 0.8 \times 10^{-3}$ μm/s, median ± MSE, $n = 15$) is also larger than that of GP ($8.5 \pm 0.39 \times 10^{-3}$ μm/s, median ± MSE, $n = 13$) ($P < 0.05$, KS test). For comparison, we recorded sequential 3-D images of immobilized 0.175-μm diameter beads under various imaging conditions. As an example, the averaged MSD plot from six beads under SNR = 6 is displayed in Fig. 5 *A*, wherein a $D^{(3)}$ of 0.087×10^{-4} μm²/s is calculated. This probably reflects our lower limit of detection under this imaging condition.

Comparing the mobility between GP and GC

In the preceding analysis, we have identified various motion types for granules according to MSD analysis, whereas detailed comparison of the 3-D mobility between GP and GC has not been made. In Fig. 6 *A*, $D^{(3)}$ distributions of 127 GPs and 119 GCs from 17 cells were compared. Because of the markedly skewed distribution, we have plotted the cumulative histogram of $D^{(3)}$ in the inset and checked the significance of difference with KS test. It is noticed that GC moves with a significant higher $D^{(3)}$ than that of GP ($P < 0.01$). Under resting conditions, 71% of GPs moved with a $D^{(3)} < 3.2 \times 10^{-4}$ μm²/s, whereas only 23.7% of GCs traveled within that $D^{(3)}$ scope. The median of $D^{(3)}$ for GPs was $2.95 \pm 0.3 \times 10^{-4}$ μm²/s ($n = 127$), which approximates the value measured for membrane-proximal granules by TIRFM (2.0×10^{-4} μm²/s, Steyer and Almers, 1999), but much lower than that of GCs ($9.5 \pm 0.9 \times 10^{-4}$ μm²/s, $n = 119$). The $D^{(3)}$ histograms of GP and GC differ significantly from a simple broad Gaussian distribution, instead featuring a markedly skewed distribution and large variation among granules. To check whether there exist distinct groups for GP and GC, we calculated the logarithmic $D^{(3)}$ distributions and displayed them in semilogarithmic presentation (Fig. 6 *B*). Two separate peaks are obvious for GP and GC, suggesting they are indeed segregated into two distinct pools based on their mobility, whereas no distinct subgroups are observed within either GP or GC (Fig. 6 *B*). Next, we compared the histograms of the radius of cage for caged diffusion between GP and GC (Fig. 6 *C*). The histogram of the radius of cage for GC extends broader to the right, and the difference in cumulative histogram comparison is significant by KS test ($P < 0.05$). GCs moved in significant larger cages with a median of 0.34 ± 0.01 μm ($n = 61$) in comparison with GP with a median of 0.22 ± 0.01 μm ($n = 69$). Finally, we found that GCs traveled a larger mean distance (scope of movement) (0.37 ± 0.04 μm, median ± MSE, $n = 127$) in three dimensions than GPs over the same observation period (0.27 ± 0.02 μm, median ± MSE, $n = 119$) ($P < 0.05$), as depicted in Fig. 6 *D*.

Stimulation increases the percentage of granules traveling in directed fashion

Most granules wandered around their residing positions in random or caged diffusion under resting condition, and only a small fraction traveled in directed fashion. We found that high K^+ (HK) stimulation significantly increased the number of granules that traveled in directed fashion for both GP and GC (Fig. 7 *A*), suggesting an up-regulated active transportation of granules. HK stimulation leads to the influx of Ca^{2+}. Ca^{2+} has been suggested to play an important role in accelerating the recruitment of secretory granules (von Rüden and Neher, 1993; Heinemann et al., 1993; Smith et al., 1998). Presumably, active transportation is involved in the recruitment of granules. Under stimulation, the median of $D^{(3)}$ was $3.6 \pm 0.5 \times 10^{-4}$ $\mu m^2/s$ ($n = 113$) and $10.3 \pm 1.3 \times 10^{-4}$ $\mu m^2/s$ ($n = 97$) for GP and GC, respectively, which were slightly higher than those of resting cells, but the differences were not statistically significant ($P > 0.35$, KS test). In contrast, the scopes of movement of GP and GC were significantly increased by HK stimulation ($P < 0.05$, Fig. 7 *C*).

The influence of actin cytoskeleton on the mobility of granules

Cortical actin cytoskeleton is localized subjacent to the plasma membrane with a thickness of ~0.4 μm (Lang et al., 2000). The mobility of granules going through the cortical actin cytoskeleton has been explored with TIRFM, whereas whether granules located inside the cell are affected by actin cytoskeleton remains less studied. Here we have employed latrunculin B (LB) to disrupt F-actin formation in PC12 cells, and performed 3-D SPT to evaluate the mobility of granules. As shown in Fig. 7 *B*, LB significantly decreased the $D^{(3)}$ of GP ($P < 0.05$, KS test) but left that of GC unaltered, suggesting actin cortex facilitates the movement of near-membrane granules rather than blocks it, which is consistent with the previous observation made by TIRFM (Lang et al., 2000). Although LB itself did not change the distribution of GPs and GCs in different motion types, the stimulatory effect of HK on the number of directed diffusion for GP was blocked by LB, an effect not seen for GC (Fig. 7 *A*). Similarly, LB blocked HK-induced increase in the scope of movement for GP but not for GC (Fig. 7 *C*). Our results suggest that although actin cytoskeleton participates actively in the movement of near-membrane granules, the trafficking of granules deep inside the cytosol is less affected by actin cytoskeleton.

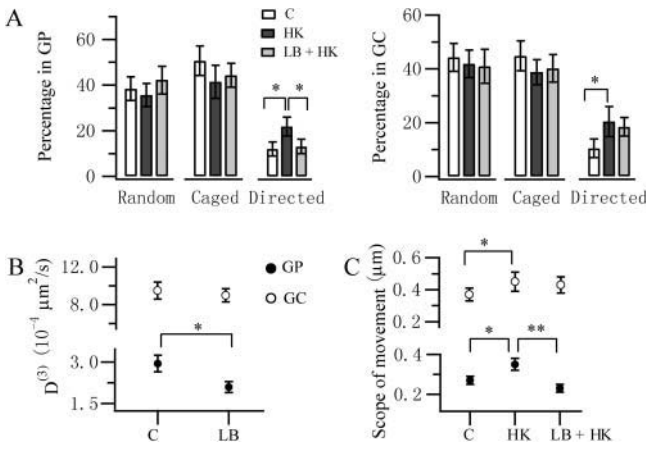

FIGURE 7 Effects of high K^+ stimulation and latrunculin-B on granule mobility. (*A*) Percentages of granules that fall into different types of motion for GP and GC. ''C'' is abbreviation for control condition, ''HK'' for high K^+ stimulation, ''LB'' for latrunculin B treatment, and ''LB + HK'' for pretreatment with LB followed by high K^+ stimulation ($n = 8$–11 cells for each condition mentioned above). (*B*) LB decreases the $D^{(3)}$ of GP significantly ($P < 0.05$, KS test) but does not change the $D^{(3)}$ of GC. (*C*) Comparison of the scope of movement for GP and GC under different conditions. For *B* and *C*, data are presented as median ± MSE, and the numbers of granules selected for analysis under various conditions are from 77 to 127 granules.

DISCUSSION

Three-dimensional granule tracking

To characterize the 3-D mobility of secretory granules throughout a whole cell, we have combined deconvolution WFFM and centroid-based 3-D SPT method to study granule trafficking in live PC12 cells. Although confocal microscopy has proved effective in removing the out-of-focus fluorescence, which improves the resolution for SPT, the inherited low time resolution limits its application in time-resolved 3-D particle tracking. Besides, confocal microscopy suffers from higher photobleaching and photodamage. In contrast, WFFM has the merit of less photobleaching and photodamage due to relatively higher light collection efficiency, especially with the highest NA (1.65) objective used in this study. The out-of-focus fluorescence in 3-D images recorded by WFFM can be computationally removed using deconvolution. In fact, WFFM combined with deconvolution has demonstrated the advantage over confocal microscopy for quantitatively studies of weakly fluorescent organelles in living cells (Swedlow and Platani, 2002).

In classical 2-D time-resolved particle tracking, the contribution from the missing axial direction is usually ignored. TIRFM-based tracking attempts to resolve the *z*-mobility from the fluctuation in granule's fluorescence that is exponentially related to the change in axial position. However, small changes in the axial position will result in large changes in fluorescence measured with TIRFM. Also, fluctuation in fluorescence unrelated to axial position will result in misinterpretation of the *z*-position. Moreover, TIRFM can only be employed to study vesicles right underneath the plasma membrane, whereas vesicles residing deeper inside the cytosol are invisible under TIRFM. Despite the recent

development in 3-D tracking of single particles (Kao and Verkman, 1994; Speidel et al., 2003; Levi et al., 2003), the 3-D mobility of granules within living cells has not been demonstrated. In this study, we have employed a centroid-based 3-D SPT from time-resolved stacks of 3-D images, and the displacements of single granules in three dimensions could be directly obtained. We found that granules can be assumed to move the same way in z direction as they behave in lateral direction, suggesting the missing z direction information in 2-D tracking probably will not impose significant distortion in assessing the lateral mobility of granules. However, 3-D tracking does offer the advantage of following granules in a larger 3-D space, not restricting to a single optical plane.

We have demonstrated that appropriate threshold selection is very critical for the precision of granule tracking. Specific threshold should be selected for each given SNR to assure the best result in 3-D tracking. We have found that higher SNRs give better accuracy in SPT, thus improving SNR will help to get better precision in granule tracking. With our NA 1.65 objective, a theoretical resolution of 0.18 μm in x, y plane and 0.45 μm in z direction is expected. The evident discrepancy between lateral and axial resolution caused by diffraction limit leads to nonisotropic resolution and precision in 3-D particle tracking. In fact, we found that the threshold optimized (optimizing procedure, see Fig. 2) for lateral tracking performance was different from that optimized for axial tracking (data not shown) at a given SNR. Increases in resolutions along x, y directions and z direction, especially breaking the distortion occurred in z direction, will balance the tracking performance in different directions. The recently developed stimulated emission depletion technique (Klar et al., 2000) and beam-scanning multifocal multiphoton 4Pi-confocal microscopy (Egner et al., 2002) have finally broken the diffraction barrier and achieved a nearly spherical resolution of $\sim$100 nm. These techniques will find more application in the demand for more precise and isotropic 3-D particle tracking. However, the drawbacks of these techniques inherited with confocal microscopy, i.e., low time resolution, high photobleaching, and photodamage, will limit their use when long-term 3-D tracking in living cell is demanded.

3-D mobility of secretory granules in PC12 cells

AO accumulates within granules as well as nonvesicular compartments like lyso- or endosome. By choosing fluorescence spots with SNR $\geq$ 6 and by applying high-pass filtering, the selected fluorescence spots has single Gaussian profiles in fluorescence with lateral and axial FWHMs indistinguishable from those of NPY-DsRed labeled dense-core granules, suggesting we were mainly analyzing AO-labeled large dense-core granules in this study. AO-loaded granules are much brighter than NPY-DsRed labeled ones, as 5 ms exposure of AO-loaded granules gave similar SNR to that of NPY-DsRed labeled granules with 100 ms exposure time (Fig. 3 *C*). Thus, the advantage of AO is not only its ease of use, but also the less exposure time and hence less photodamage. PC12 cells are densely packed with secretory granules. Our selection criteria might exclude most of the weakly stained spots (i.e., small synaptic like vesicles) and large spots for analysis; however, $\sim$65% of the observed granules remained for analysis after selection. Moreover, although the density of our selected AO-labeled granules ($0.12 \pm 0.02/\mu m^2$) is lower than that of NPY-labeled granules observed under TIRFM ($0.358/\mu m^2$, Taraska et al., 2003) in PC12 cells, it is comparable with the density of cytosolic granules in chromaffin cells observed using electron microscopy ($0.11/\mu m^2$, Steyer et al., 1997).

The characterization of particle motion imposes demands on the temporal and spatial resolution required for the measurement. When there is only simple free diffusion, as indicated by the linear dependence of MSD on time, the time resolution of the measurement does not influence the determination of the diffusion coefficient from the slop of the plot of MSD($n\Delta t$). In contrast, when diffusion is constrained by a cage or tether, a characteristic time of observation is required together with a corresponding requirement for sufficient temporal resolution to resolve the dynamic motion (Qian et al., 1991). Previous study has suggested that granules wander rapidly with a diffusion coefficient of $19 \times 10^{-4}\ \mu m^2/s$ within a cage that leaves $\sim$70 nm space around granules, whereas the cage itself diffuses in random 10-fold more slowly over longer distances (Steyer and Almers, 1999). The slow effective sampling rate (0.2 Hz) used in this study due to 3-D stack generation will miss the fine movement of granules within the cage. However, it will accurately track the long range diffusion of granules, which presumably reflects the movement of the cage.

Imaging under TIRFM is restricted to a thin layer underneath the plasma membrane, which adheres unphysiologically to the coverglass. Whether the adhesion of plasma membrane to coverglass will affect the mobility of neighboring granules and their fusion remains to be examined. Interestingly, we found that GPs residing far away from the basal plasma membrane exhibit similar diffusion coefficient as that measured by TIRFM (Steyer and Almers, 1999, Becherer et al., 2003). GP in this study also traveled in a similar cage as that observed under TIRFM. Along with the fact that diffusion of fluorescent dyes could be observed as a ''cloud'' after fusion, it is likely the adhesion of basal membrane to coverglass does not exert significant effect on the surrounding granules.

Secretory granules have long been assumed to belong to distinct functional pools (Bratanova-Tochkova et al., 2002; Duncan et al., 2003). By simultaneously tracking near-membrane and cytosolic granules, we have found significant differences between these two groups of granules in their $D^{(3)}$, radius of cage, and scope of movement. The mobility of these two groups of granules is also differentially affected by

disruption of F-actin. These results suggest that the motion of the two groups of granules is mediated by different mechanisms. However, we failed to distinguish subgroups within either GPs or GCs. The distributions of diffusion coefficient for either GP or GC did not exhibit multiple distinct peaks, suggesting granules are smoothly organized into one population, rather than into distinct pools, and most of them travel with lower mobility. This result is consistent with a recent study in the neurites of differentiated PC12 cells under TIRFM by Ng et al. (2003), who reported a broad and asymmetric distribution in diffusion coefficient without a separation of a distinct pool of granules. With the advantage of our method to study the mobility of granules deep inside the cytosol, we now extend this feature to cytosolic granules.

Correlation of granules with cortical actin cytoskeleton

Although some granules wandered with random diffusion, granule trafficking is likely to be mediated by different cytoskeleton systems along with a number of motor proteins (Hirokawa, 1998; Kamal and Goldstein, 2002). Thus, the motion of single granules might be influenced by expected or unexpected organelles on their way. The caged diffusion of granules much adjacent to the plasma membrane has been previously elucidated by TIRFM (Steyer and Almers, 1999; Oheim and Stühmer, 2000; Johns et al., 2001), which is seen as the entrapment of granules inside the cortical actin cytoskeleton meshwork. In this study, we have found that besides near-membrane granules, a majority of cytosolic granules traveled in a caged fashion as well. Interestingly, lots of GCs are likely trapped in a larger cage than GPs, suggesting a relatively looser meshwork inside cytosol. In addition to its role in restricting the movement of granules, cytoskeleton meshwork has also been thought to actively participate in granule motion, as well as to supply directional tracks for granule transportation (Rogers and Gelfand, 2000; Lang et al., 2000). In this study, we did find a small fraction of granules traveling in a directed fashion. Stimulation with HK solution increased the number of granules in directed traveling as well as the velocity of directed traveling (data not shown), whereas the diffusion coefficients remained unchanged, indicating an increased impelling of granules in an active manner. The augmentation in directed traveling was significantly inhibited by disruption of actin cytoskeleton for GP, but not for GC (Fig. 7 *A*). Moreover, the $D^{(3)}$ and the scope of movement of GP were also more prone to the treatment of LB than those of GC (Fig. 7, *B* and *C*). Taking together, we propose that the movement of near-membrane granules are likely mediated as well as constrained by cortical actin network, whereas cytoskeleton other than cortical actin participates in the movement of cytosolic granules. Further experiments are demanded to identify the correlations between granule mobility and the underlying molecular mechanisms employing similar techniques used in this study.

We thank J. Yao and T. Liang for assistance in the cell preparation, L. Xu and L. Bai for help in the adjustment of the imaging system, and J. Ding for helpful comments on the manuscript.

This work was supported by National Science Foundation of China Grants No. 60071030 to A. Qu, Nos. 30025023, 3000062, and 30130230 to T. Xu, and National Basic Research Program of China (973) Grant G1999054000 and 2001CCA04100 to T. Xu. We are grateful for the support from the Li Foundation and the Sinogerman Scientific Center. The laboratory of T. Xu belongs to a Partner Group Scheme of the Max Planck Institute for Biophysical Chemistry, Göttingen, Germany.

REFERENCES

Angleson, J. K., A. J. Cochilla, G. Kilic, I. Nussinovitch, and W. J. Betz. 1999. Regulation of dense core release from neuroendocrine cells revealed by imaging single exocytic events. *Nat. Neurosci.* 2:440–446.

Avery, J., D. J. Ellis, T. Lang, P. Holroyd, D. Riedel, R. M. Henderson, J. M. Edwardson, and R. Jahn. 2000. A cell-free system for regulated exocytosis in PC12 cells. *J. Cell Biol.* 148:317–324.

Becherer, U., T. Moser, W. Stuhmer, and M. Oheim. 2003. Calcium regulates exocytosis at the level of single vesicles. *Nat. Neurosci.* 6:846–853.

Bratanova-Tochkova, T. K., H. Cheng, S. Daniel, S. Gunawardana, Y. Liu, J. Mulvaney-Musa, T. Schermerhorn, S. G. Straub, H. Yajima, and G. W. G. Sharp. 2002. Triggering and augmentation mechanisms, granule pools, and biphasic insulin secretion. *Diabetes.* 51:s83–s90.

Canny, J. 1986. A computational approach to edge detection. *IEEE Trans. Pattern Anal. Mach. Intell.* 8:679–698.

Cheezum, M. K., W. F. Walker, and W. H. Guilford. 2001. Quantitative comparison of algorithms for tracking single fluorescent particles. *Biophys. J.* 81:2378–2388.

Conchello, J. A., and J. G. McNally. 1996. Fast regularization technique for expectation maximization algorithm for computational optical sectioning microscopy. *In* Three-Dimensional Microscopy: Image Acquisition and Processing. Proc. 1996 IS & T/SPIE Symposium on Electronic Imaging: Science and Technology. C. J. Cogswel, G. Kino, and T. Wilson editors. SPIE—The International Society for Optical Engineering, SPIE code No. 2655–24, Bellingham, WA.

Duncan, R. R., J. Greaves, U. K. Wiegand, L. Matskevich, G. Bodammer, D. K. Apps, M. J. Shipston, and R. H. Chow. 2003. Functional and spatial segregation of secretory vesicle pools according to vesicle age. *Nature.* 422:176–180.

Egner, A., S. Jakobs, and S. W. Hell. 2002. Fast 100-nm resolution three-dimensional microscope reveals structural plasticity of mitochondria in live yeast. *Proc. Natl. Acad. Sci. USA.* 99:3370–3375.

Gibson, S. F., and F. Lanni. 1991. Experimental test of an analytical model of aberration in an oil-immersion objective lens used in three-dimensional light microscopy. *J. Opt. Soc. Am. A. Opt. Image Sci. Vis.* 9:154–166.

Gosh, R. N., and W. W. Webb. 1994. Automated detection and tracking of individual and clustered cell surface low density lipoprotein receptor molecules. *Biophys. J.* 66:1301–1318.

Heinemann, C., L. von Rüden, R. H. Chow, and E. Neher. 1993. A two-step model of secretion control in neuroendocrine cells. *Pflugers Arch.* 424:105–112.

Hirokawa, N. 1998. Kinesin and dynein superfamily proteins and the mechanism of organelle transport. *Science.* 279:519–526.

Holroyd, P., T. Lang, D. Wenzel, P. D. Camilli, and R. Jahn. 2002. Imaging direct, dynamin-dependent recapture of fusing secretory granules on plasma membrane lawns from PC12 cells. *Proc. Natl. Acad. Sci. USA.* 99:16806–16811.

Jahn, R., T. Lang, and T. C. Südhof. 2003. Membrane Fusion. *Cell.* 112:519–533.

Johns, L. M., E. S. Levitan, E. A. Shelden, R. W. Holz, and D. Axelrod. 2001. Restriction of secretory granule motion near the plasma membrane of chromaffin cells. *J. Cell Biol.* 153:177–190.

Kamal, A., and L. S. Goldstein. 2000. Connecting vesicle transport to the cytoskeleton. *Curr. Opin. Cell Biol.* 12:503–508.

Kamal, A., and L. S. Goldstein. 2002. Principles of cargo attachment to cytoplasmic motor proteins. *Curr. Opin. Cell Biol.* 14:63–68.

Kao, H. P., and A. S. Verkman. 1994. Tracking of single fluorescent particles in three dimensions: use of cylindrical optics to encode particle position. *Biophys. J.* 67:1291–1300.

Klar, T. A., S. Jakobs, M. Dyba, A. Egner, and S. W. Hell. 2000. Fluorescence microscopy with diffraction resolution barrier broken by stimulated emission. *Proc. Natl. Acad. Sci. USA.* 97:8206–8210.

Kues, T., A. Dickmanns, R. Luhrmann, R. Peters, and U. Kubitscheck. 2001. High intranuclear mobility and dynamic clustering of the splicing factor U1 snRNP observed by single particle tracking. *Proc. Natl. Acad. Sci. USA.* 98:12021–12026.

Lang, T., I. Wacker, J. Steyer, C. Kaether, I. Wunderlich, T. Soldati, H.-H. Gerdes, and W. Almers. 1997. Ca2+-triggered peptide secretion in single cells imaged with green fluorescent protein and evanescent-wave microscopy. *Neuron.* 18:857–863.

Lang, T., I. Wacker, I. Wunderlich, A. Rohrbach, G. Giese, T. Soldati, and W. Almers. 2000. Role of actin cortex in the subplasmalemmal transport of secretory granules in PC-12 cells. *Biophys. J.* 78:2863–2877.

Leung, Y. M., L. Sheu, E. Kwan, G. Wang, R. Tsushima, and H. Gaisano. 2002. Visualization of sequential exocytosis in rat pancreatic islet β cells. *Biochem. Biophys. Res. Commun.* 292:980–986.

Levi, V., Q. Ruan, K. Kis-Petikova, and E. Gratton. 2003. Scanning FCS, a novel method for three-dimensional particle tracking. *Biochem. Soc. Trans.* 31:997–1000.

Levitan, E. S. 1998. Studying neuronal peptide release and secretory granule dynamics with green fluorescent protein. *Methods.* 16:182–187.

Markham, J., and J. A. Conchello. 1997. Tradeoffs in regulated maximum-likelihood image restoration. *In* 3D Microscopy: Image Acquisition and Processing IV. Proc. of the 1997 SPIE's Biomedical Optics Symposium, BiOS97. C. J Cogswel., J. A. Conchello, and T. Wilson, editors. SPIE—The International Society for Optical Engineering, SPIE code No 2984–18, Bellingham, WA.

Ng, Y.-K., X. Lu, A. Gulacsi, W. Han, M. J. Saxton, and E. S. Levitan. 2003. Unexpected mobility variation among individual secretory vesicles produces an apparent refractory neuropeptide pool. *Biophys. J.* 84:4127–4134.

Ohara-Imaizumi, M., Y. Nakamichi, T. Tanaka, H. Ishida, and S. Nagamatsu. 2002. Imaging exocytosis of single insulin secretory granules with evanescent wave microscopy. *J. Biol. Chem.* 277:3805–3808.

Oheim, M., and W. Stühmer. 2000. Tracking chromaffin granules on their way through the actin cortex. *Eur. Biophys. J.* 29:67–89.

Ölveczky, B. P., N. Periasamy, and A. S. Verkman. 1997. Mapping fluorophore distributions in three dimensions by quantitative multiple angle-total internal reflection fluorescence microscopy. *Biophys. J.* 73: 2836–2847.

Pfeffer, S. R. 1999. Transport-vesicle targeting: tethers before SNAREs. *Nat. Cell Biol.* 1:E17–E22.

Pouli, A. E., E. Emmanouilidou, C. Zhao, C. Wasmeier, J. C. Hutton, and G. A. Rutter. 1998. Secretory-granule dynamics visualized in vivo with a phogrin-green fluorescent protein chimaera. *Biochem. J.* 333:193–199.

Qian, H., M. P. Sheetz, and E. L. Elson. 1991. Single particle tracking. Analysis of diffusion and flow in two-dimensional systems. *Biophys. J.* 60:910–921.

Rogers, S. L., and V. I. Gelfand. 2000. Membrane trafficking, organelle transport, and the cytoskeleton. *Curr. Opin. Cell Biol.* 12:57–62.

Saxton, M. J., and K. Jacobson. 1997. Single-particle tracking: applications to membrane dynamics. *Annu. Rev. Biophys. Biomol. Struct.* 26:373–399.

Smith, C., T. Moser, T. Xu, and E. Neher. 1998. Cytosolic Ca^{2+} acts by two separate pathways to modulate the supply of releasable-competent vesicles in chromaffin cells. *Neuron.* 20:1243–1253.

Speidel, M., A. Jonas, and E. Florin. 2003. Three-dimensional tracking of fluorescent nanoparticles with subnanometer precision by use of off-focus imaging. *Opt. Lett.* 28:69–71.

Steyer, J. A., and W. Almers. 1999. Tracking single secretory granules in live chromaffin cells by evanescent-field fluorescence microscopy. *Biophys. J.* 76:2262–2271.

Steyer, J. A., H. Horstmann, and W. Almers. 1997. Transport, docking and exocytosis of single secretory granules in live chromaffin cells. *Nature.* 388:474–478.

Swedlow, J. R., and M. Platani. 2002. Live cell imaging using wide-field microscopy and deconvolution. *Cell Struct. Funct.* 27:335–341.

Taraska, J. W., D. Perrais, M. Ohara-Imaizumi, S. Nagamatsu, and W. Almers. 2003. Secretory granules are recaptured largely intact after stimulated exocytosis in cultured endocrine cells. *Proc. Natl. Acad. Sci. USA.* 100:2070–2075.

Thompson, R. E., D. R. Larson, and W. W. Webb. 2002. Precise nanometer localization analysis for individual fluorescent probes. *Biophys. J.* 82: 2775–2783.

Toonen, R. F. G., and M. Verhage. 2003. Vesicle trafficking: pleasure and pain from SM genes. *Trends Cell Biol.* 13:177–186.

Tooze, S. A., T. Flatmark, J. Tooze, and W. B. Huttner. 1991. Characterization of the mature secretory granule, an intermediate in granule biogenesis. *J. Cell Biol.* 115:1491–1503.

von Rüden, L., and E. Neher. 1993. A Ca-dependent early step in the release of catecholamines from adrenal chromaffin cells. *Science.* 262: 1061–1065.